

# Military jet noise source imaging using multisource statistically optimized near-field acoustical holography

Alan T. Wall<sup>a)</sup>

*Air Force Research Laboratory, Battlespace Acoustics Branch, Wright-Patterson Air Force Base, Dayton, Ohio 45433, USA*

Kent L. Gee and Tracianne B. Neilsen

*Department of Physics and Astronomy, N283 ESC, Brigham Young University, Provo, Utah 84602, USA*

Richard L. McKinley

*Air Force Research Laboratory, Battlespace Acoustics Branch, Wright-Patterson Air Force Base, Dayton, Ohio 45433, USA*

Michael M. James

*Blue Ridge Research and Consulting, LLC, Asheville, North Carolina 28801, USA*

(Received 21 May 2015; revised 24 March 2016; accepted 27 March 2016; published online 19 April 2016)

The identification of acoustic sources is critical to targeted noise reduction efforts for jets on high-performance tactical aircraft. This paper describes the imaging of acoustic sources from a tactical jet using near-field acoustical holography techniques. The measurement consists of a series of scans over the hologram with a dense microphone array. Partial field decomposition methods are performed to generate coherent holograms. Numerical extrapolation of data beyond the measurement aperture mitigates artifacts near the aperture edges. A multisource equivalent wave model is used that includes the effects of the ground reflection on the measurement. Multisource statistically optimized near-field acoustical holography (M-SONAH) is used to reconstruct apparent source distributions between 20 and 1250 Hz at four engine powers. It is shown that M-SONAH produces accurate field reconstructions for both inward and outward propagation in the region spanned by the physical hologram measurement. Reconstructions across the set of engine powers and frequencies suggests that directivity depends mainly on estimated source location; sources farther downstream radiate at a higher angle relative to the inlet axis. At some frequencies and engine powers, reconstructed fields exhibit multiple radiation lobes originating from overlapped source regions, which is a phenomenon relatively recently reported for full-scale jets. [<http://dx.doi.org/10.1121/1.4945719>]

[JWP]

Pages: 1938–1950

## I. INTRODUCTION

The need for the mitigation of noise from high-performance tactical aircraft increases the importance of understanding the nature of the acoustic sources. Measurements and models of coherent wave-like turbulent structures have been widely investigated as the dominant source of mixing noise in high-speed jets. Detailed analyses of the sound field in the vicinity of tactical aircraft provide equivalent acoustic source representations. Efforts are underway to correlate equivalent acoustic sources to turbulent source mechanisms.<sup>1,2</sup> In addition, data-educed source distributions can be used to predict the radiated field. In this paper, reconstructions of the noise sources in a full-scale heated supersonic jet are obtained using a near-field acoustical holography (NAH)<sup>3</sup> approach.

Mollo-Christensen<sup>4</sup> observed correlated regions in the sound near jet flows as early as 1967 and modeled them with an analytical function (wavepacket). This model represented a spatially correlated source with a characteristic wave number, phase speed, and amplitude modulation (downstream growth and decay). These properties have become tenets of

jet noise modeling efforts. Tam<sup>5</sup> linked the directional acoustic radiation to the growth and decay of instability waves in the jet shear layer. Tam<sup>6</sup> later pointed out the importance of the source amplitude modulation, in that such modulation broadens the radiated wave number spectrum, and then proposed that the relation between the peak radiation direction and the source phase speed is the same as the relation between the direction of Mach wave radiation and the speed of a supersonically traveling wavy wall. The idea linking the peak radiation direction of a jet to a characteristic phase speed, or convection velocity, is important for the analyses in this paper.

Although direct measurements of jet noise sources made within the shear layer would be ideal, the temperature, flow speed, and harsh environment of full-scale tactical jets introduces formidable challenges. Acoustic imaging techniques based on near-field microphone arrays are a practical alternative. Previous array measurements of tactical jets are limited. In one notable study, Schlinker *et al.*<sup>7</sup> used a 30-microphone phased array to estimate the source regions of a full-scale supersonic jet engine. They showed source distributions the maximum locations of which were almost invariant with frequency; this differed from their laboratory-scale results and the laboratory-scale distributions obtained in other studies.<sup>8–10</sup>

<sup>a)</sup>Electronic mail: [alantwall@gmail.com](mailto:alantwall@gmail.com)

However, because the phased array they used had a small aperture that covered a limited portion of the field, the resulting full-scale source distributions corresponded only with sound energy radiated to the array location.

In 2009, extensive, array-based measurements were made of an F-22A Raptor with more than 6000 measurement points from the near to the mid field.<sup>11</sup> In past investigations, Harker *et al.*<sup>12,13</sup> used the 50-microphone linear array from this dataset (i.e., the reference array shown in Sec. II) and a beamforming approach that incorporates source coherence to produce source magnitude distributions. Similar trends in source distribution were obtained from subsets of this dataset using an equivalent source model (ESM) approach<sup>14</sup> and with a ray-tracing method based on near-field vector intensity measurements.<sup>15</sup> Neilsen *et al.*<sup>16</sup> demonstrated spectral characteristics of the F-22A that deviated from typical laboratory-scale jet spectra, such as shallower high-frequency spectral slopes than lab-scale data, and spectral shapes typical of fine-scale turbulence in the far downstream region.

In this paper, NAH is used to generate high-resolution reconstructions of the tactical jet noise sources and sound fields using the data measured near an F-22A. Past researchers have performed NAH on lab-scale jets,<sup>8,9,17–20</sup> and these studies provided useful insights into the relations between source and field properties. Initial cylindrical NAH reconstructions of the F-22A were recently made using the linear 50-microphone array.<sup>21</sup> A key advantage of NAH over other imaging methods, such as beamforming, wavepacket modeling,<sup>22</sup> or other ESM methods, is that it requires minimal assumptions about source distribution (such as amplitude modulation), coherence, or wave speed; rather, a measure of these features can be obtained from an NAH source reconstruction. Because NAH requires coherent holograms as inputs, partial field decomposition (PFD) must be performed, and the resulting mutually incoherent partial fields are projected independently.<sup>23</sup> The NAH reconstructions of the full-scale jet in the present paper validate the source properties estimated by previous investigations of the F-22A, allow for additional analyses of source and field properties, and even provide an explanation for the discrepancy between the Schlinker *et al.*<sup>7</sup> full-scale jet source distributions and lab-scale data.

The current work builds on the previous F-22A studies by providing reconstructions of the full-scale jet acoustic source distributions for various engine conditions and frequencies using multisource statistically optimized near-field acoustical holography (M-SONAH).<sup>24</sup> In this paper, Sec. II provides a summary of the noise measurements conducted near a tethered F-22A Raptor. Section III outlines the methodology of sound field reconstructions performed in this study, including PFD of the hologram data, numerical extrapolation of data beyond the measurement aperture, and the formulation of the field equivalent wave model (EWM) used in the NAH projection that accounts for reflections from a rigid ground. This section also includes a validation of the methodology wherein field reconstructions are compared to benchmark measurements. In Sec. IV, reconstructed levels are shown in the geometric near field of the F-22A, and equivalent source models are provided for four engine powers over a broad frequency range. The relations between source and radiation features, and what they

indicate about the flow properties, are discussed. A summary of key results and recommendations for future jet investigations are provided in Sec. V. The Appendix contains a numerical exercise that demonstrates a method for determining M-SONAH reconstruction regions of low error.

## II. EXPERIMENT

In 2009, static run-up tests were conducted on the Lockheed Martin/Boeing F-22A Raptor, the details of which can be found in Ref. 11. The F-22A Raptor has two Pratt and Whitney F119-PW-100 turbofan engines, each with a rectangular nozzle aspect ratio of about 2:1, and each of which is capable of 160 kN (35 000 lbf) of thrust. The nozzle exits are complicated by the presence of movable thrust vectoring paddles. The center of each nozzle was 1.9 m (75 in.) above the ground. With the aircraft tethered to a run-up pad, the engine nearest the measurement arrays was cycled through IDLE, intermediate (INT), military (MIL), and afterburner (AB) engine powers. The other engine was held at IDLE throughout. The concrete run-up pad was 24.4 m (80 ft) wide with rain-packed dirt on either side. The dominant source of reflections in the measurement was the run-up pad. The effects of temperature fluctuations and wind speeds were determined to be minor over the short propagation distances in this measurement (<23 m), as explained in Ref. 9.

The F-22A experiment is the most extensive near-field measurement of a jet on a high-performance military aircraft to date. Figure 1(a) shows the holography array as it performs a “scan” near the F-22A at high power. The holography array consisted of 90 prepolarized microphones arranged in a  $5 \times 18$  regular grid with spacing of 0.15 m (6 in.). Figure 1(b)

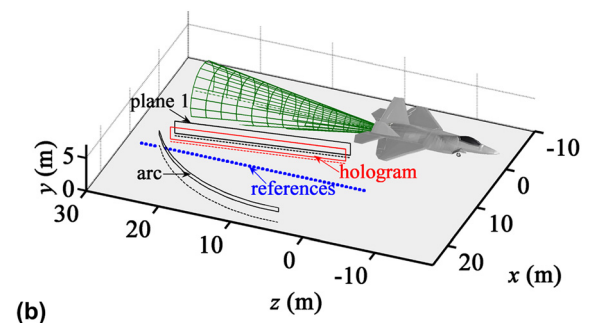


FIG. 1. (Color online) (a) Photograph of the 90-microphone array in one of the scan positions adjacent to the aircraft. (b) Schematic of the measurement locations relative to the aircraft.

shows a schematic of the total measurement. The origin of the coordinate system is on the ground directly below the nozzle exit. The planar hologram surface shown in Fig. 1(b) consisted of 30 scans by the array (10 horizontal, 3 vertical) in both horizontal and vertical directions and was aligned parallel to and 5.6 m from the estimated shear layer boundary. A second planar measurement was made at a closer offset distance of 4.1 m [called plane 1 in Fig. 1(b)]. Plane 1 represents the closest possible measurements to the exhaust due to the fact that the peak pressures of the sound field approached the upper limit of the dynamic range of the microphones. To enable the generation of coherent holograms from mutually incoherent scans, 50 reference microphones were placed along the ground, parallel to the jet centerline, at  $x = 11.6$  m, with regular 0.61-m (2-ft) spacing. In addition, for benchmarking purposes, seven measurement scans were taken along a 22.9 m (75 ft) arc centered on the estimated maximum source location, defined as 5.5 m (18 ft) downstream of the nozzle exit.

### III. METHODOLOGY

The successful application of NAH to high-performance tactical aircraft noise built on previous NAH techniques but required several modifications to the methodology used in less extreme settings. The holography process begins with a PFD of the scan data to create partial fields, which are then numerically extrapolated beyond the measurement aperture. The M-SONAH process, in which the formulation of the field EWM used in the NAH projection accounts for reflections from a rigid ground, is then applied to the hologram and the sound field can be projected to any location. To validate the method, field reconstructions are compared to benchmark measurements.

#### A. The holography process

To guide the reader in the following description of the method of implementing M-SONAH on the full-scale jet data, the procedure is summarized as follows.

- (1) Extract complex pressures from recorded pressure waveforms.
- (2) Perform PFD to generate mutually incoherent partial fields.
- (3) Numerically extrapolate each partial field beyond the measurement aperture.
- (4) Reduce the grid resolution of each partial field.
- (5) Formulate the EWM of the jet in the run-up pad environment.
- (6) Project the pressures of each partial field to desired locations.
- (7) Sum the projected partial fields energetically.

Each of these steps is detailed in the following text.

First, complex pressures were computed. A Fourier transform was taken of recorded time blocks that were windowed with a Hanning function and overlapped 50%. Time-block lengths were large enough to ensure that blocks recorded simultaneously at the hologram plane and along the reference array, with some microphones tens of meters apart, could be adequately compared for coherence; the

simultaneous blocks had at least 90% overlap based on a time delay resulting from an assumed sound speed of 343 m/s. This overlap is necessary for the accurate estimation of cross spectra, which is integral to the PFD processing discussed in the following text. The Fourier processing was repeated for all scans over the hologram, reference, and benchmark locations and for all engine conditions. The complex pressures corresponding to the preferred center frequencies of one-third-octave bands were extracted from the narrowband spectra. The remainder of the processing was performed on each one-third-octave band-center frequency independently.

A self-coherent hologram is required in an NAH projection. Hence for the second step, PFD based on singular value decomposition (SVD) of the reference array cross-spectral matrix was performed. Variations in the source level from scan to scan were accounted for using the methods of Lee and Bolton.<sup>25</sup> It should be noted that although the virtual coherence method<sup>26</sup> can be used to find an optimized cutoff for singular values of the reference cross-spectral matrix, it requires that the reference array capture all source-related energy measured by the hologram. Because the reference array of the current experiment was limited to the ground, some of the signal coherent with information at the top of the hologram (far from the ground) was not captured by the references for the highest frequencies investigated here. It was difficult to use virtual coherence to optimize the cutoff singular values at the frequencies where the reference array was insufficient, so all singular values after the tenth were forced to zero to filter out spatial measurement noise. The effects of this truncation are observable in the high-frequency reconstructions shown in the following subsection. For future jet noise measurements, Wall *et al.*<sup>27</sup> have provided guidelines for sufficient reference arrays for partially coherent sources. All subsequent steps were performed independently on each partial field up to the point where the partial fields were summed to obtain the total fields.

The SONAH algorithm<sup>28</sup> was originally developed in part to relax the requirement for a measurement aperture that extends far beyond the edges of a source as is required in conventional NAH. Thus, at least when the standoff distance of the hologram from the source is very small, SONAH reconstruction artifacts from the data truncation at the edges are insignificant. For the current experiment, transducers could not be placed any closer than several meters, and the relatively large propagation distances would result in significant edge-related artifacts if the measured hologram data were used directly. To mitigate the effects of aperture windowing, in the third step the hologram partial fields were numerically extrapolated. Note that the purpose of the aperture extension was not to restore or predict actual field information missed by the array, which is discussed separately in Sec. III A.

In preparation for this work, several extrapolation methods were investigated for their ability to represent physically realistic data immediately outside of the measurement aperture.<sup>29</sup> Linear forward prediction was chosen for its relatively high accuracy in numerical experiments and its computational efficiency. For the current experiment, the

accuracy of the data predicted outside of the aperture cannot be determined, but the extrapolated fields do taper gracefully toward zero away from the aperture edge; this is a condition that helps to mitigate artifacts in the reconstructions.<sup>30</sup>

In linear forward prediction,<sup>31</sup> the coefficients of a polynomial are determined from existing data, and the polynomial is then used to predict data beyond the original aperture. In the current study, the complex pressure data along a given row of a partial field were used to determine the coefficients of the polynomial, and the value of the polynomial immediately beyond the last point of the row was taken as the first data point outside the aperture. Then the entire row of data, including the first extrapolated point, was used to find a polynomial and predict the second extrapolated point. This process was repeated to extend the aperture about 20 m in both the upstream and downstream directions for all rows of all partial fields. Then a Tukey window was applied to the extended data to reduce reconstruction artifacts that result from non-physical predictions far from the measurement aperture edge. The Tukey window was defined to have a value of 1 at the measurement aperture edge and to decay to 0 within two acoustic wavelengths. No vertical extrapolation was necessary because the sound field was modeled with axisymmetric modes that do not require a large azimuthal aperture,<sup>32</sup> hence, doing so had a negligible effect on results.

The fourth step was to reduce the hologram grid resolution for increased computational speed. The greatest factor in computational time for the M-SONAH algorithm, as well as the memory requirements, is the number of points in the hologram. To capture all possible wave functions used in the EWM of this experiment, measured by a uniformly spaced hologram, there must be at least two microphones per wavelength; to capture near-field (evanescent) information, this is the wavelength that represents (models) the size of source features rather than the acoustic wavelength. The lower frequencies investigated here do not require a hologram with the dense spacing at which these measurements were taken (0.15 cm). Hence, rows and columns of the data are removed after the aperture extension, such that there are at least four hologram points per acoustic wavelength, where possible. For the highest frequency investigated (1250 Hz), there were slightly fewer than two hologram points per acoustic wavelength, but because the majority of energy was obliquely incident on the array, the two-microphone-per-wavelength criterion was met for the trace wavelength along the array.<sup>33</sup>

Fifth, the EWM used in the M-SONAH algorithm was formulated to represent the jet in the presence of the ground reflection. This approach was validated in a previous numerical study<sup>33</sup> and in an implementation of the method on the F-22A for a single frequency and engine power.<sup>34</sup> The EWM included one set of cylindrical wave functions centered on the jet centerline and a second set centered on the image source created by the reflection. The current experiment motivated the development of the M-SONAH method,<sup>24</sup> and the formulation here is performed accordingly. It is important to understand that the M-SONAH method is employed to increase the accuracy of sound field reconstructions with the source in the presence of the reflecting surface, not to

remove the effect and obtain a free-field estimate of a source model. McLaughlin *et al.*<sup>35</sup> performed a study that showed free-field estimates of jet noise radiation from measurements made with a nearby reflecting surface are possible under certain conditions, but discrepancies between their model and measurement highlight the challenges that arise when the full physics of the problem is not understood. The effort to overcome these challenges for the current data set is beyond the scope of the current paper, although free-field equivalent source estimates may be possible in the future using M-SONAH or similar techniques, along with carefully designed measurements in the presence of ground reflections.

Cylindrical wave functions for outward propagating waves are defined as

$$\Phi_{\ell,k_z}(r, \phi, z) \equiv \frac{H_{\ell}^{(1)}(k_r r)}{H_{\ell}^{(1)}(k_r r_0)} e^{i\ell\phi} e^{ik_z z}, \quad r \geq r_0, \quad (1)$$

where  $r$ ,  $\phi$ , and  $z$  are the radial, azimuthal, and axial spatial coordinates, respectively;  $H_{\ell}^{(1)}$  is the  $\ell$ th-order Hankel function of the first kind;  $i$  represents the imaginary unit;  $r_0$  is some small reference radius (traditionally the assumed source radius);<sup>36</sup> and  $k_z$  is the axial wavenumber. The radial wavenumber,  $k_r$ , is then constrained by

$$k_r = \begin{cases} \sqrt{k^2 - k_z^2}, & \text{for } |k| \geq |k_z|, \\ i\sqrt{k_z^2 - k^2}, & \text{for } |k| < |k_z|, \end{cases} \quad (2)$$

where  $k$  is the acoustic wavenumber,  $\omega/c$ ,  $\omega$  is the angular frequency, and  $c$  is the speed of sound.

Two wave function sets were chosen to represent the jet source and its image in the EWM. The wave function sets are defined in Table I, along with the necessary equations to transform from the Cartesian coordinates of Fig. 1(b) to the respective coordinates used in each wave function and the orders and coordinate-specific wave numbers included in each set. The vector  $\mathbf{r} = (r, \phi, z)$  in Table I represents a local coordinate in the respective wave function set,  $\mathbf{r}_h$  corresponds to positions of the set of hologram points (after aperture extension and grid reduction), and  $\mathbf{r}_q$  is the set of locations at which the sound field is to be reconstructed.

TABLE I. Definition of two wave function sets designed to represent a jet source and its image source.

|   |
|---|
| $\mathbf{B}_1 \equiv [\Phi_{\ell,k_z}(\mathbf{r}_h)]$ and $\boldsymbol{\beta}_1 \equiv [\Phi_{\ell,k_z}(\mathbf{r}_q)]$ , where<br>$r \equiv \sqrt{x^2 + (y - 1.9\text{m})^2}$<br>$\phi \equiv \tan^{-1}\left(\frac{y - 1.9\text{m}}{x}\right)$ , four-quadrant arctangent with range $(-\pi, \pi]$<br>$z \equiv z$<br>$\ell = 0$<br>$\Delta k_z = \pi/L_z,  k_z _{\max} = 2\pi/\Delta z$ |
| $\mathbf{B}_2 \equiv [\Phi_{\ell,k_z}(\mathbf{r}_h)]$ and $\boldsymbol{\beta}_2 \equiv [\Phi_{\ell,k_z}(\mathbf{r}_q)]$ , where<br>$r \equiv \sqrt{x^2 + (y + 1.9\text{m})^2}$<br>$\phi \equiv \tan^{-1}\left(\frac{y + 1.9\text{m}}{x}\right)$ , four-quadrant arctangent with range $(-\pi, \pi]$<br>$z \equiv z$<br>$\ell = 0$<br>$\Delta k_z = \pi/L_z,  k_z _{\max} = 2\pi/\Delta z$ |

Thus,  $\mathbf{B}_1$  and  $\mathbf{B}_2$  are the hologram wave function matrices for the jet and image sources, respectively, and  $\boldsymbol{\beta}_1$  and  $\boldsymbol{\beta}_2$  are the respective reconstruction matrices. In Table I, the wave-number spacing,  $\Delta k_z$ , and the wavenumber extrema,  $|k_z|_{\max}$ , are specified by the axial aperture length,  $L_z$ , and the axial sample spacing,  $\Delta z$ , according to the recommendations of Hald.<sup>37</sup> Each wave function matrix has a number of rows equal to the number of wave functions and a number of columns equal to the number of hologram or reconstruction points. The total EWM matrices are formed by concatenating the two sets of wave functions for the hologram and reconstruction locations, respectively, as

$$\mathbf{A} = \begin{bmatrix} \mathbf{B}_1 \\ \mathbf{B}_2 \end{bmatrix} \quad \text{and} \quad \boldsymbol{\alpha} = \begin{bmatrix} \boldsymbol{\beta}_1 \\ \boldsymbol{\beta}_2 \end{bmatrix}. \quad (3)$$

Note that only the azimuthal order  $\ell = 0$  is included because the EWM is restricted to the axisymmetric mode. The limited azimuthal coverage of the measurement made the representation of higher orders inaccurate. This does not mean that higher orders are not important to model the jet, only that the array could not accurately capture them. In essence, a limited amount of information about the equivalent acoustic source was gained by the vertical extent of the aperture. However, the vertical aperture does capture salient features of the interference pattern<sup>11</sup> that are essential for modeling how the source behaves in the presence of the ground reflection.<sup>14,38</sup>

With the EWM defined, the sixth step of sound field propagation was performed. At this point the M-SONAH processing becomes identical to SONAH.<sup>37</sup> The projected pressures at the reconstruction locations are

$$\mathbf{p}(\mathbf{r}_q) = \mathbf{p}^T(\mathbf{r}_h) \mathbf{R}_{\mathbf{A}^H \mathbf{A}} \mathbf{A}^H \boldsymbol{\alpha}, \quad (4)$$

where superscript H is the Hermitian transpose,  $\mathbf{p}^T(\mathbf{r}_h)$  is the transpose of the complex pressures on the hologram, and  $\mathbf{R}_{\mathbf{A}^H \mathbf{A}}$  is the regularized inverse of  $\mathbf{A}^H \mathbf{A}$ . Regularization was performed using the modified Tikhonov filter in conjunction with the generalized cross-validation (GCV) procedure for the selection of the regularization parameter.<sup>39</sup>

Both inward propagation and outward propagation are presented. To benchmark the accuracy of the NAH process, reconstructions are made at plane 1 and at the arc. Reconstructions that model the geometric near field are made in the  $x$ - $z$  plane at a height of  $y = 1.9$  m, equal to the height of the jet centerline and near the head height of aircraft maintainers. Apparent source distributions were estimated by sound pressure levels (SPLs) reconstructed along the jet axis at a distance of  $x = 0.3$  m (one-half of the nozzle hydraulic diameter) from the jet centerline and at a height of  $y = 1.9$  m.

Last, the squared pressures of all partial fields are summed to obtain the total fields. For the measurements and reconstructions shown, all narrowband pressures at the preferred one-third-octave band-center frequencies are scaled on the assumption that they represent the energy contained in the entire one-third-octave band and are transformed to a sound pressure level (SPL) according to the equation

$$\text{SPL} = 10 \log_{10} \left( \frac{p^2 \left( \frac{\Delta f_{1/3}}{\Delta f} \right)}{(20 \mu\text{Pa})^2} \right), \quad (5)$$

where  $\Delta f_{1/3}$  is the bandwidth of the respective one-third octave band,  $\Delta f$  is the bandwidth of the Fourier-transformed narrow bands, and  $20 \mu\text{Pa}$  is the root-mean-square reference pressure. This scaling approximates the true one-third-octave spectra because the narrowband spectrum tends to be broadband and smooth, with no strong tonal content in the frequency range spanned in the current analysis. Evidence of the lack of tonal content is found in the work of Neilsen *et al.*,<sup>16</sup> who showed that the F-22A spectra, at the polar angles discussed here, are dominated by jet mixing noise, which is highly broadband in nature. Due to restrictions on the permissible use of these data, the analyses here were not performed for frequencies sampled more densely than at one-third-octave bands.

## B. Validation

Two methods are employed here to validate the reconstructions. First, reconstructions are compared directly to measured SPLs (benchmarks) where data are available. Both inward and outward reconstructions are compared to benchmarks. The benchmark comparison is the more critical of the two validation approaches. The secondary validation is based on a numerical investigation, and it provides a method to estimate the spatial regions of low reconstruction error where benchmark data are not available. This numerical study is located in the Appendix. The final acoustic source reconstructions shown in Sec. IV are truncated to the regions of estimated low error based on the results of the numerical study.

The ability of the M-SONAH algorithm to reconstruct the field closer to the source, referred to as inward reconstruction, is evaluated via comparisons with benchmark measurements along the row of plane 1 at  $y = 1.9$  m. At high frequencies, reflections from the array rig resulted in spatial measurement noise, so benchmark data are filtered using a moving average along the rows, with a span of 9 points (equal to one-half of the 18 points along each row of the array). Spatial filtering in the NAH processing eliminates the need for post-filtering of reconstruction results. In Fig. 2(a), benchmark SPLs are shown as a function of one-third-octave band center frequency and downstream location,  $z$ , as identified in Fig. 1(b). Contour lines are separated by 2 dB with thick contour lines at 10 and 20 dB below the maximum level. Figure 2(b) contains the reconstructed levels at the same locations. The reconstruction captures the salient features of the field and is accurate to within 1 dB at most locations. An exception occurs downstream of  $z = 22$  m, where the energy shown in the benchmark is not present in the reconstruction because the physical measurement aperture did not extend far enough downstream. Because of the directional nature of the sound propagation, noise components far downstream on plane 1 are not captured on plane 2. An underestimation also occurs at high frequencies because some high-frequency energy was not included in the PFD

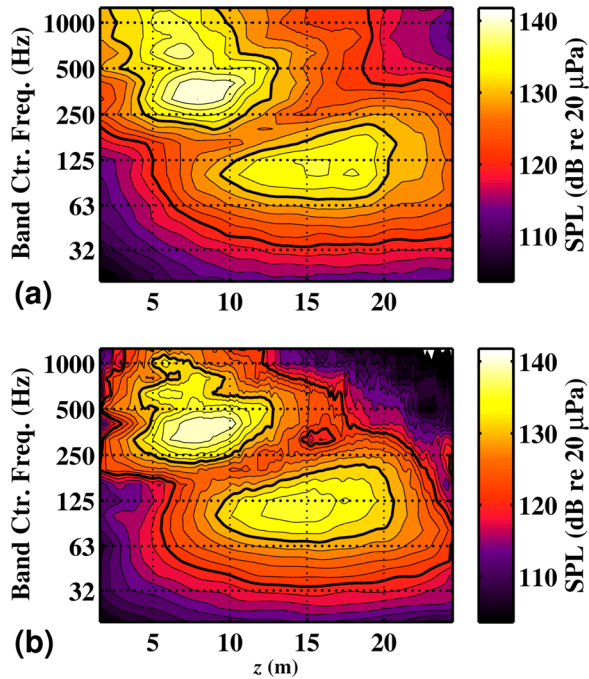


FIG. 2. (Color online) (a) One-third-octave band spectral variation at MIL power along the row of plane 1 at a height of 1.9 m. (b) Total M-SONAH reconstructions at the same locations and frequencies. Contour lines occur at 2 dB increments with thick lines at 10 and 20 dB below the maximum level of the benchmark.

due to the insufficiency of the reference array, as described in Sec. III A. However, note that the reconstruction does capture the maximum energy at 1000 Hz within 2 dB as well as the location of the maximum. The underestimation becomes more pronounced as spatial distance from the maximum region increases.

Note the multi-lobed nature of the sound field, characterized by multiple local maxima in the spatial/frequency domain of Fig. 2. In this figure, the nulls between local maxima are dominated by destructive interference due to ground reflections. However, the F-22A sound field also exhibits multi-lobed radiation independent of the presence of the ground. This was first pointed out in Ref. 11 and will be discussed further in Sec. IV.

A summary of inward reconstruction accuracy is provided by a comparison of mean level differences and peak-to-peak level differences between the reconstruction and benchmarks along the same locations shown in the preceding text. Figure 3(a) shows the value of the reconstructed SPLs averaged across  $z$  minus the benchmark SPLs averaged across  $z$  along the row of plane 1 at  $y = 1.9$  m for all engine conditions and frequencies. The mean errors all tend to be underpredictions (negative values), and their magnitudes are less than 5 dB up to 500 Hz, above which the missing energy in the PFD causes the reconstructions to deviate. However, the peak-level errors shown in Fig. 3(b), calculated as the difference in SPL between the maximum values of the SPLs from the reconstruction and the benchmark (not necessarily at the same spatial location; this emphasizes the differences in field intensities rather than their relative distributions), remain less than 5 dB (or 2 dB for MIL and AB powers) for

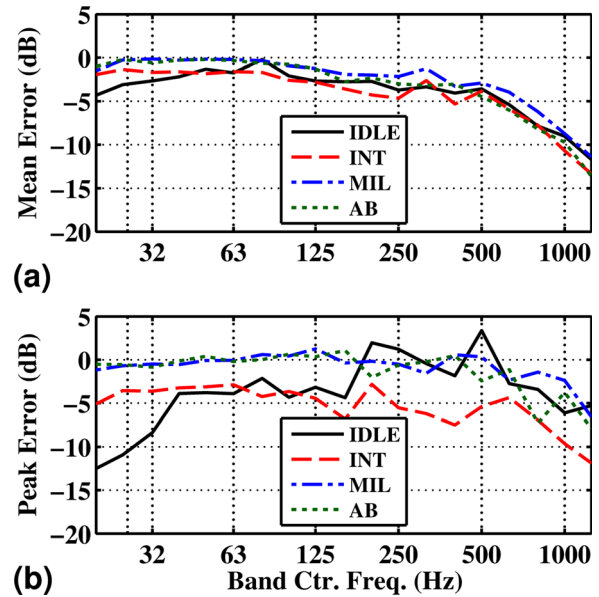


FIG. 3. (Color online) Errors between the NAH reconstructions and SPL measured along the row of plane 1 at a height of 1.9 m. (a) Mean difference in SPLs and (b) difference between the peak value of the reconstruction and the peak value of the benchmark.

most frequencies up to the maximum frequency. The INT condition is characterized by unusually large errors because the source was less stationary;<sup>11</sup> no set throttle position exists for the pilot to operate the aircraft at INT power, so the source at this condition was more susceptible to human error. The magnitudes of the INT partial fields resulting from the PFD were smooth and settled toward values within the range measured during the scans. The peak-level errors for IDLE are largest at 160 Hz and below because the source was about 5 dB louder (more for the lowest frequencies) for one benchmark scan than the other nine scans. The averaging used to obtain the IDLE error in Fig. 3(a) minimizes this effect.

To quantify outward propagation accuracy, benchmark and reconstructed SPLs at the arc (see Fig. 1), along the row at  $y = 1.9$  m, are shown for MIL power in Fig. 4. The angle  $\theta$  is defined with respect to the center of the arc (5.5 m downstream of the nozzle exit) and measured from the inlet axis. At the arc, the maximum levels of the predicted sound field at high frequencies are also accurate within about 2 dB, and accuracy degrades at the edges of the measurement aperture. Note that the shallow null in the 200-Hz region is not due to destructive interference as it was in Fig. 2—the same null occurs in the measurements made by the ground-based reference array.<sup>11</sup> It is important to note that at sideline angles near  $90^\circ$  and  $100^\circ$ , and below about 600 Hz, the reconstructions are still accurate to within about 2 dB even though this region is most likely dominated by fine-scale turbulent mixing noise.<sup>16</sup> Recent attempts to estimate far-field jet noise radiation using analytical wavepacket models have successfully predicted noise in the downstream region where radiation from large-scale turbulence dominates, but they have sometimes been unable to predict sideline levels.<sup>40,41</sup> The current reconstructions show that sideline levels can be represented using NAH techniques. In theory, so long as

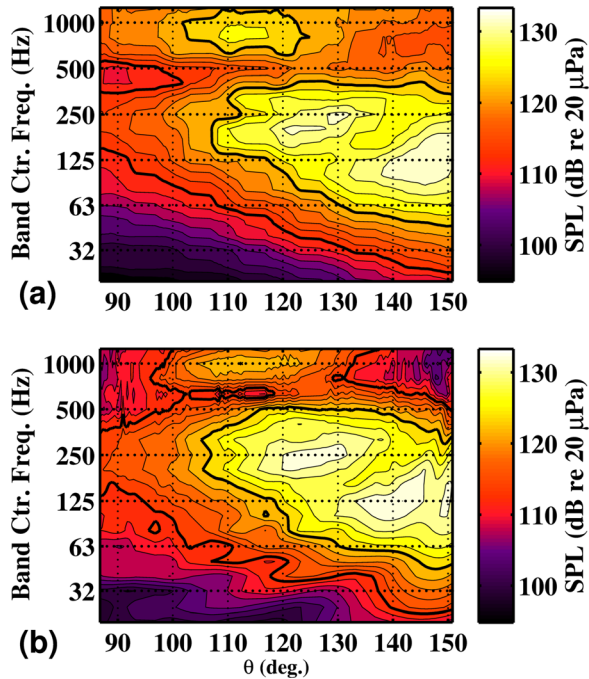


FIG. 4. (Color online) (a) One-third-octave band spectral variation at MIL power over location along the row of the arc at a height of 1.9 m and a distance of 22.9 m. Angles are measured relative to the engine inlet. (b) Total M-SONAH reconstructions at the same locations and frequencies. Contour lines occur at 2 dB increments with thick lines at 10 and 20 dB below the maximum level of the benchmark.

minimum array requirements are met, NAH can be used to reconstruct sources of any scale, resolution, and coherence.

A summary of the accuracy of the outward propagation is displayed in Fig. 5. The mean errors between the data and the reconstruction along the row of the arc at  $y = 1.9$  m are shown for all engine conditions and frequencies in Fig. 5(a), and the peak-level errors are shown in Fig. 5(b). In a similar

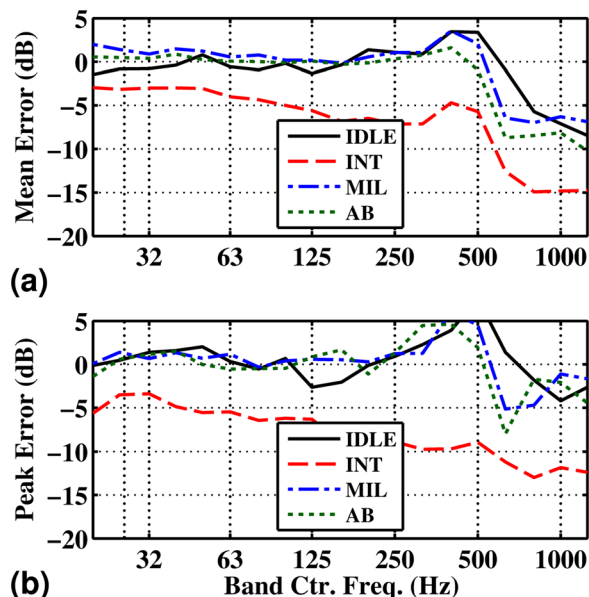


FIG. 5. (Color online) Errors between the NAH reconstructions and SPL measured along the row of the arc at a height of 1.9 m. (a) Mean difference in SPLs and (b) difference between the peak value of the reconstruction and the peak value of the benchmark.

manner to the inward case, outward propagation mean errors are mainly within 2 dB of zero below 315 Hz and then increase; peak-level errors at the highest frequencies remain mostly less than 5 dB. The cause of outward propagation overestimates near 500 Hz for all engine powers can be deduced from Fig. 4. Figure 4(a) shows that a shallow interference null occurs along most of the arc at 500 Hz. By comparison, the reconstruction in Fig. 4(b) places the null closer to 630 Hz. This may result from small differences between the center locations of the cylindrical functions used in the holography EWM and the “actual” acoustic center of the (volumetric) jet flow. Again, the levels at INT power are consistently underpredicted due to source nonstationarity.

#### IV. RESULTS

M-SONAH reconstructions of the jet acoustic field were performed for all one-third-octave band frequencies between 20 and 1250 Hz at all four engine powers (IDLE, INT, MIL, and AB). An example of a horizontal planar field reconstruction in the jet vicinity at 125 Hz with the aircraft operating at MIL power is shown in Fig. 6 at a height  $y = 1.9$  m from a three-dimensional perspective. The strong directionality of the radiation is evident. Before evaluating the source reconstructions, a series of field reconstructions on this same surface at different frequencies and engine conditions are examined.

In Figs. 7–10, two-dimensional, top-down views of the field reconstructions are shown for the four engine powers at selected frequencies between 32 and 1000 Hz. On all images, the  $x$ - $z$  location of the physical hologram is shown by a solid line. Features of the reconstructed field beyond the edges of the hologram are likely due to artifacts that occur because of sound energy not measured in that region. However, most salient features of the field occur well within the hologram region.

The effects of the ground reflecting plane are accounted for in the two-source EWM used in the M-SONAH algorithm. These effects can be seen in the interference patterns of the reconstructed fields in Figs. 7–10, with nulls running nearly parallel to the  $z$  axis. The interference would not be present in a free-field measurement, but previous studies have shown that a model of sources along the jet centerline and along its reflected image accurately locate the interference nulls and peaks in this environment.<sup>14</sup>

Although the physical jet flow characteristics for the F-22A are unknown, the equivalent acoustic observations of the current section can be tied to properties of physical jets (or physical acoustic sources in general) based on historical efforts linking the two. For example, the directivity of a spatially extended acoustic source is dependent on its phase speed. Equivalent acoustic models of jets often include a phase-speed parameter, and attempts have been made to equate the phase speed with the convective velocity of a jet instability wave.<sup>4,40,42,43</sup> It is understood that phase speed, and hence direction of radiation, may be influenced by factors other than jet convective velocity, most clearly evidenced by the fact that subsonic jets produce directional radiation at all.<sup>40,44</sup> However, in the current discussion, it is

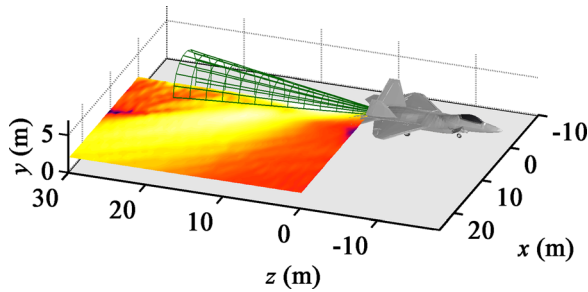


FIG. 6. (Color online) M-SONAH reconstruction at 125 Hz in the vicinity of the jet at MIL power. Levels are shown over a planar surface at  $y = 1.9$  m, the height of the centerline of the jet.

assumed that some deterministic relationship exists between convection velocity and directivity, which is a broadly accepted hypothesis.

Between 32 and 250 Hz for the IDLE reconstructions of Fig. 7, it is questionable whether the noise is generated by jet mixing sources. It is possible that the sources are radiating somewhat omnidirectionally from a region near the nozzle exit, but the aperture truncation effects render such a conjecture difficult. Measured spectra of the F-22A at IDLE power<sup>45</sup> do not exhibit the common “haystack” shape typical in jet noise measurements. However, perhaps at 500 Hz and certainly at 1000 Hz, the IDLE field in Fig. 7 takes on a directional nature with a strong lobe pointing almost to the sideline. It is well known that subsonic jets

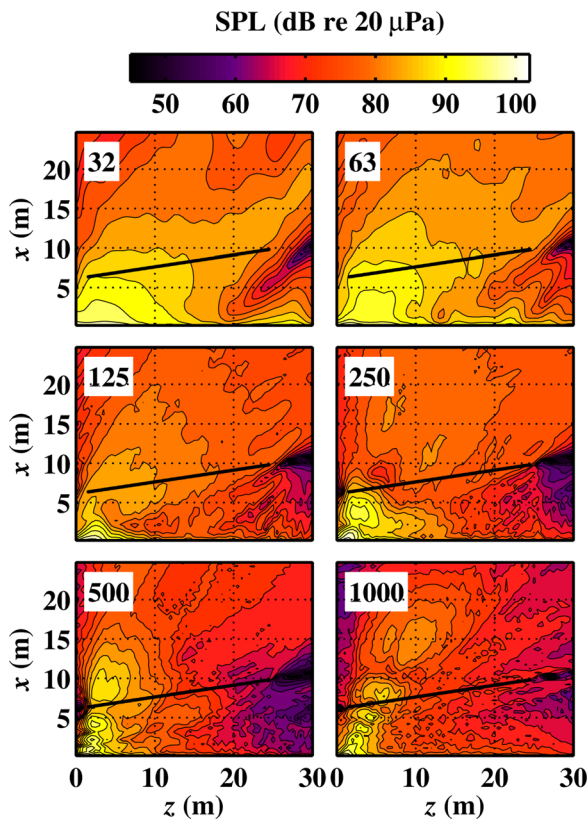


FIG. 7. (Color online) Frequency-dependent reconstructions of the acoustic field radiated from the F-22A with both engines operated at IDLE power, over a horizontal plane at a height of  $y = 1.9$  m. Frequencies are shown in the top left of each map. Contour lines are separated by 3 dB. The solid line delineates the location of the hologram.

exhibit Mach-wave-like radiation, although the mechanisms of its production are debated.<sup>41,44</sup> The fact that the low-speed flow at IDLE power is characterized by directional radiation at angles this far forward is surprising and merits further investigation.

At INT and higher engine powers, it is clear that jet mixing noise dominates any other aircraft or extraneous noise sources.<sup>16</sup> At all frequencies for these powers, the reconstructed fields are characterized by strong lobes with well-defined directionality. For each engine power in Figs. 8–10, the maximum source region and the radiation lobe shift from downstream locations and aft directions to closer to the nozzle and more toward the sideline as frequency increases. In addition, at most frequencies, the lobe directionality shifts from downstream toward the upstream as engine power increases. An example can be seen in a comparison of the 125-Hz field across Figs. 8–10; the field maxima for this frequency along “slices” taken at  $x = 15$  m occur near  $z = 25$ , 22, and 19 m for INT, MIL, and AB powers, respectively. It is well understood that the velocity of the jet slows with distance from the nozzle.<sup>46</sup> The relationship between the apparent source maximum location and directivity for the full-scale jet shown here is consistent with a convection velocity that decreases with distance downstream and increases with engine power, in contrast to the full-scale results shown by Schlinker *et al.*<sup>7</sup>

Although the jet source directivity shifts toward the sideline with increasing frequency, this may not necessarily be a continuous spatial transition. To demonstrate this, the MIL power field reconstructions are repeated in Fig. 11, but this

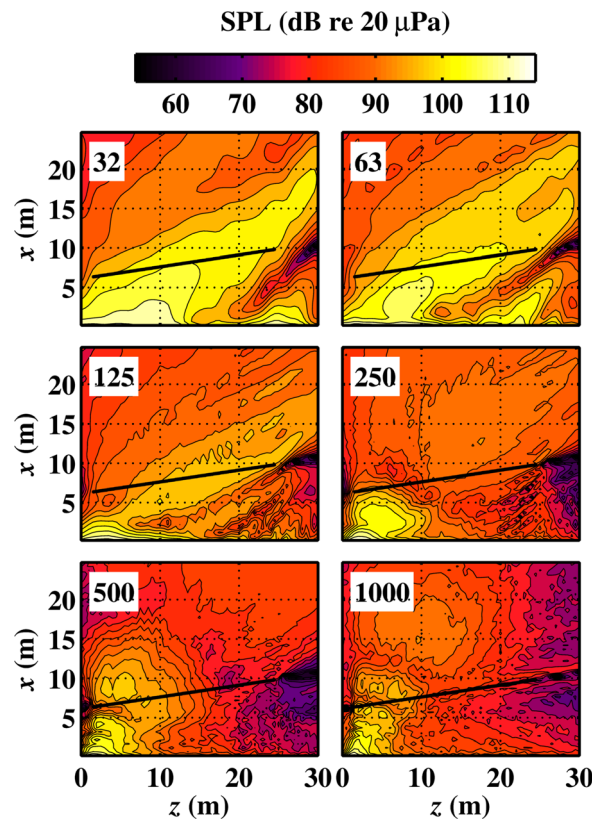


FIG. 8. (Color online) Similar to Fig. 7 but with one engine operated at INT power.

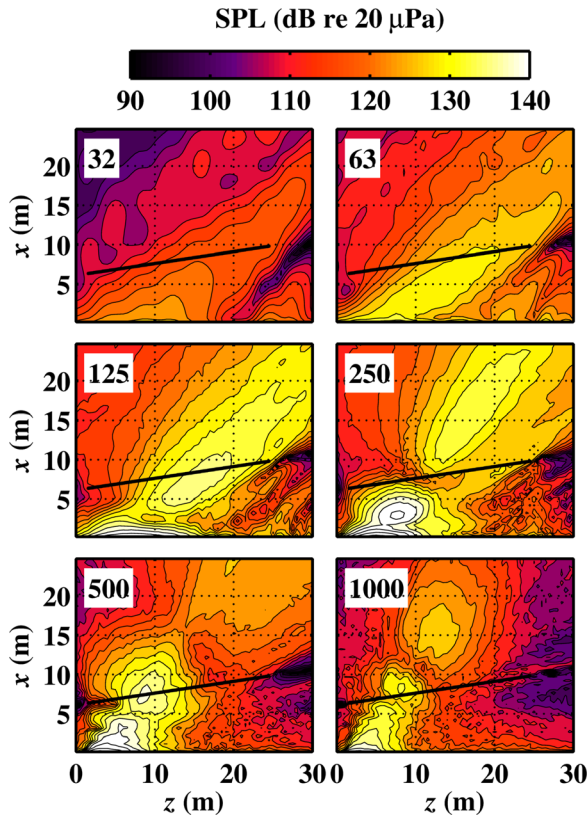


FIG. 9. (Color online) Similar to Fig. 7 but with one engine operated at MIL power.

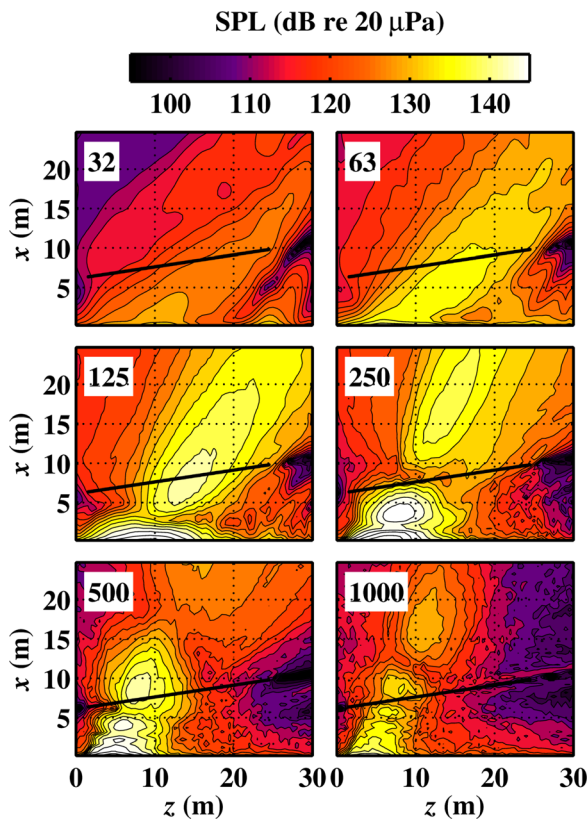


FIG. 10. (Color online) Similar to Fig. 7 but with one engine operated at AB power.

time for all one-third-octave bands between 125 and 400 Hz. The main lobes from 32 to 125 Hz (in Fig. 9) all point far aft, toward the approximate location of  $(z, x) = (30, 20)$  m. However, in Fig. 11, between 160 and 250 Hz, this aft lobe is shown to grow weaker with increasing frequency, while a second lobe emerges pointing toward  $(25, 25)$  m. At 315 Hz, this second lobe is joined by a third lobe farther forward, pointing toward  $(20, 25)$  m, and at 400 Hz, the third lobe is the dominant feature. A similar behavior exists at AB power. This multi-lobe radiation is a seemingly ubiquitous feature of full-scale jets<sup>7,47,48</sup> that has only recently been pointed out.<sup>11,16</sup> Although no conclusive explanation of multi-lobe radiation has been discussed in past investigations, the idea has been treated in several past studies. Tam and Parrish<sup>49</sup> sought to explain the additional spectral peaks of the F-22A in terms of indirect combustion noise sources that originate from within the nozzle, but the reconstructions shown here place the equivalent acoustic sources several meters downstream. Liu *et al.*<sup>50</sup> show, in a large-eddy simulation of an underexpanded jet, an aft noise lobe in addition to the Mach wave radiation lobe and ascribe this second lobe to the maximum contribution of the shock-associated noise. In Figs. 13, 15, and 16 of Ref. 50, a striation pattern is shown in the axial/frequency domain that results from the shock-cell noise component and is consistent with the behavior of the multi-lobe radiation shown here for the F-22A. In an NAH experiment of

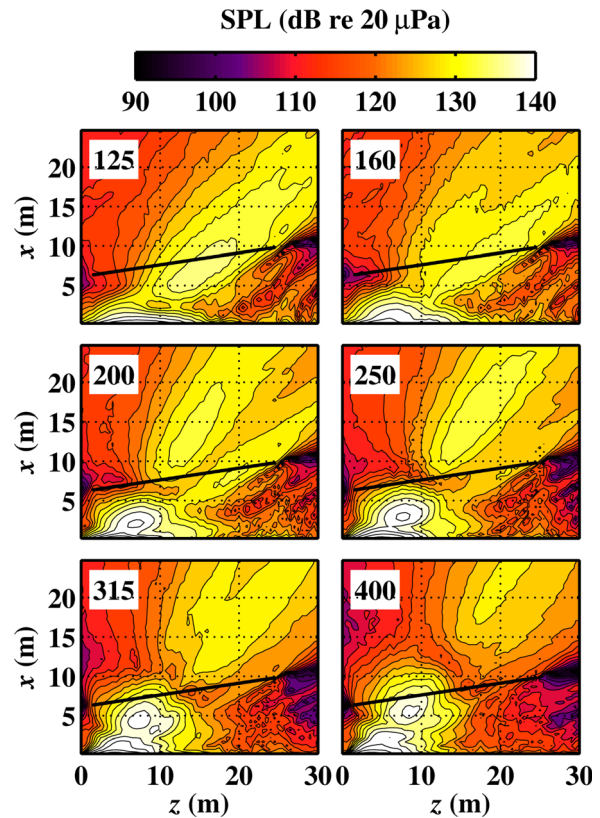


FIG. 11. (Color online) Frequency-dependent reconstructions of the acoustic field radiated from the F-22A with one engine operating at IDLE power and the other at MIL power, over a horizontal plane at a height of  $y = 1.9$  m, and at all one-third-octave band center frequencies from 125 to 400 Hz. Frequencies are shown in the top left of each map. Contour lines are separated by 3 dB. The solid line delineates the location of the hologram.

a high-speed, heated, laboratory-scale jet by Long *et al.*,<sup>8</sup> similar striations were shown to match the locations of shock cells when imaged at the source. The results of these latter two studies point toward shock cell interactions as the most likely cause of the multi-lobe radiation of the F-22A. Another possible contribution to the pattern is suggested in a follow-on study where Liu *et al.*<sup>51</sup> simulated a high-temperature supersonic jet free of shock cells and demonstrated two noise components that suggest Mach wave radiation and large-scale turbulence radiation may be distinct phenomena rather than two descriptors of the same source mechanism.

The M-SONAH reconstructions in Fig. 12 provide models of the equivalent pressure field in the source region,

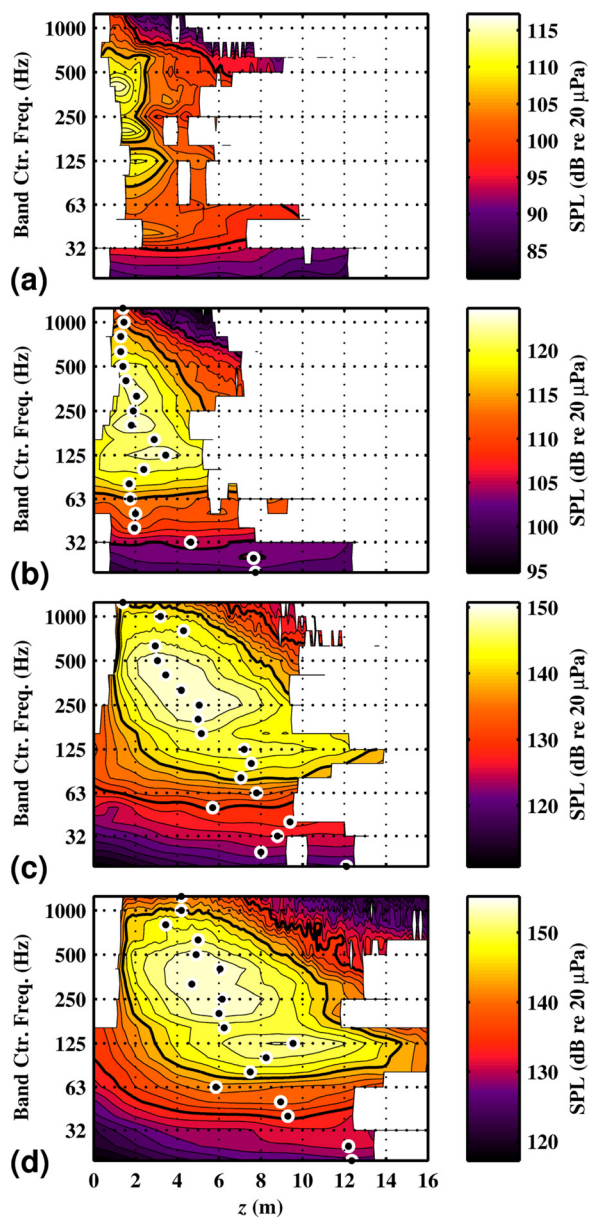


FIG. 12. (Color online) Reconstructed apparent source distributions as a function of one-third-octave band for (a) IDLE, (b) INT, (c) MIL, and (d) AB engine conditions. Contour lines occur at 2 dB increments with thick lines at 10 and 20 dB below the maximum level. Dots mark the location of the maximum level at each frequency (not shown for IDLE). Results are truncated for each frequency based on the change in level covered by the hologram aperture as explained in the Appendix.

specifically along the equivalent nozzle lip line (defined here as one-half of the hydraulic diameter) as a function of  $z$  and of frequency (20–1250 Hz) for all four engine powers. Note that no flow data are available, so no attempt is made here to correlate equivalent acoustic source data with the turbulent flow of the jet beyond the qualitative relationships that have been shown in previous works. Acoustic source data are truncated according to the truncation-level criterion explained in the appendix, where the truncations on the upstream and downstream sides have been treated independently and each frequency is treated independently (i.e., there is a different truncation level for each frequency, found by the method given in the Appendix). Note that no such truncation is applied to the two-dimensional field reconstructions of Figs. 7–10. Based on the analysis of Sec. III B (see Fig. 3), it is expected that for MIL and AB source reconstructions below 500 Hz are accurate to within 2 dB with uncertainties reaching approximately 5 dB for INT engine power and around the peak-level locations at the highest frequencies. Uncertainties at the high frequencies increase as distance from the location of the maximum level increases. Thus for all engine conditions, above about 500 Hz, the locations of the acoustic source maxima shown in Fig. 12 are accurately represented, but the distributions should be broader than those shown.

A dot shows the locations of maximum level for each frequency in Fig. 12. In the case of IDLE power, the hologram may not have extended far enough upstream to capture the source maxima, so a discussion about source distributions is difficult, but the maxima appear to be closer to the nozzle than 2 m. In the cases of INT, MIL, and AB, most of the energy within the top 10 dB was captured, and trends in the location of the source maximum with frequency can be seen. In general, the source distributions become less compact and the source maximum moves downstream as either the frequency decreases or the engine power increases, consistent with source reconstructions of laboratory jets.<sup>8–10</sup> Because the directivity of the sound field exhibits a similar relationship—directionality tends to point farther downstream with a decrease in frequency or a decrease in engine power—this corroborates the idea that local mean convective velocity rather than an overall velocity is the main influence on directionality. A dependence on the estimation of a single convection velocity may be a weakness in several wavepacket models.<sup>4,40,42</sup> In addition, based on the relation between source location and directivity, the reason Schlinker *et al.*<sup>7</sup> showed a supersonic jet source distribution the maximum location of which did not vary with frequency may have been because they only measured the field at one location, which was dominated by sound radiation from one sub-region within the jet.

In the case of MIL and AB power, note that the multiple spatial lobes seen in Fig. 11 are not visible in Fig. 12(c); the lobes coalesce as they approach the source region. Thus either self-coherent, multi-pole-like source mechanisms or spatially overlapping, independent sources result in multiple discrete directionalities. The studies of Stout *et al.*<sup>15</sup> and Harker *et al.*<sup>13</sup> showed low mutual coherence between the two main lobe regions in the mid field, suggesting that the

lobes might be independent. The coherence of the multiple lobe features will be the focus of future investigations.<sup>52</sup>

## V. CONCLUDING DISCUSSION

Acoustical holography techniques have been used to reconstruct field and equivalent source pressures of a full-scale tactical aircraft jet. The M-SONAH method was employed to account for the measurement in the presence of ground reflections. The sound field was represented by the superposition of two sets of cylindrical wave functions, one centered on the jet and the second centered on the image source. Comparisons of reconstructions to benchmark measurements demonstrated the accuracy of the field imaging. A technique was proposed to identify, based on the SPLs captured by the physical hologram measurement, the regions of reliable source reconstruction (see the [Appendix](#)).

Comparisons across engine conditions and over a range of frequencies show that the equivalent acoustic source location and directionality shift downstream and aft with decreasing engine power (INT through AB) and decreasing frequency. A convective velocity that decreases with distance downstream can explain this phenomenon, suggesting that the dominant influence on source directivity is the local convective velocity near the maximum source region.

An important difference exists between the IDLE reconstructions and the results for higher engine powers. Although it is unclear whether the sources at IDLE are dominated by jet mixing noise or some other mechanism, the 1000-Hz (and possibly 500-Hz) field reconstruction exhibits a directional lobe far forward with respect to the jet axis, almost to the sideline. This surprising result requires further investigation.

Another interesting result of the M-SONAH reconstructions was that for some frequencies and engine powers, the reconstructed field exhibited multiple, distinct lobes of radiation that converged to spatially overlapping regions at the source. These multiple lobes have only recently been reported as a prevalent aspect of high-power military aircraft with limited to no discussion in the context of laboratory-scale jets. However, existing laboratory jet data showing spatial/spectral maps of the radiated field point toward regularly spaced shock cell structures as a possible contributor to the lobing patterns. For example, a direct comparison was made of radiation lobes to shock cell locations by Long *et al.*<sup>9</sup> In future investigations, spatial coherence calculations between the lobe features will be used to determine whether the fields are caused by coherently interfering sources or independent sources radiating in different directions. Preliminary efforts in this regard can be found in Ref. 52.

Although the current experiment represents the most extensive measurement of a full-scale jet to date, the measurement aperture did not span the entire source region for all the frequencies investigated. The 27 m hologram plane did not cover the entire sound field, resulting in underestimations of reconstructed levels in the far downstream regions at low frequencies. Also, the linear reference array limited the extent to which azimuthal variation in the field

could be reconstructed. The fact that restricting the EWM to axisymmetric modes provided the most accurate result, in spite of the many previous studies that have demonstrated significant energy represented by low-order, non-axisymmetric modes, suggests that an increase in azimuthal coverage could capture more information. In spite of these limitations, reconstructions at frequencies below 500 Hz were mostly accurate to within 2 dB, and even the maximum regions of the highest frequencies, which suffered most from the limited vertical aperture, were shown to be accurate within about 5 dB.

The generation of an ESM for the F-22A from these data is beyond the scope of this paper. The technical challenges that must first be overcome include the current limitation of the holographic reconstruction to 1250 Hz and below (because of array element spacing), limited azimuthal coverage, and the fact that only one of the two engines was fired for most engine powers. The strength of the NAH methods used here lies in their ability to provide detailed inward and outward reconstructions of the sound field that lead to insights into characteristics of the acoustic sources and radiation. It is anticipated that future efforts to generate ESMs for full-scale jets might include combinations of holography, wavepacket modeling, beamforming, and acoustic vector intensity techniques.

Results from this experiment provide important guidance for improved holographic measurements of full-scale jets in the future. For example, axial coverage would likely be sufficient if the top 20 or 30 dB of energy were captured over all frequencies of interest rather than in an overall sense. To increase the highest frequencies that can be imaged, both the hologram and reference array apertures should extend farther in the azimuthal direction to allow more azimuthal modes in the model; a sufficient coverage could be estimated using principles of spatial coherence similar to those found in Refs. 27 and 32. In Sec. III A, the need was discussed for overlap in the time blocks of hologram and reference microphones such that coherence between the two sets could be accurately estimated. In a physical measurement of a large source, such as a full-scale jet, near-field arrays should span tens of meters. For scan-based measurements, it is recommended that the reference array be as close as possible to the hologram array to minimize the time delays between the two.

## ACKNOWLEDGMENT

The authors gratefully acknowledge funding from the U.S. Air Force Research Laboratory (USAFRL) through the SBIR program and support through a Cooperative Research and Development Agreement among Blue Ridge Research and Consulting, Brigham Young University, and the Air Force. This research was supported in part by the appointment of A.T.W. to the Postgraduate Research Participation Program at the U.S. Air Force Research Laboratory, 711th Human Performance Wing, Human Effectiveness Directorate, Warfighter Interface Division, Battlespace Acoustics Branch administered by the Oak Ridge Institute for Science and

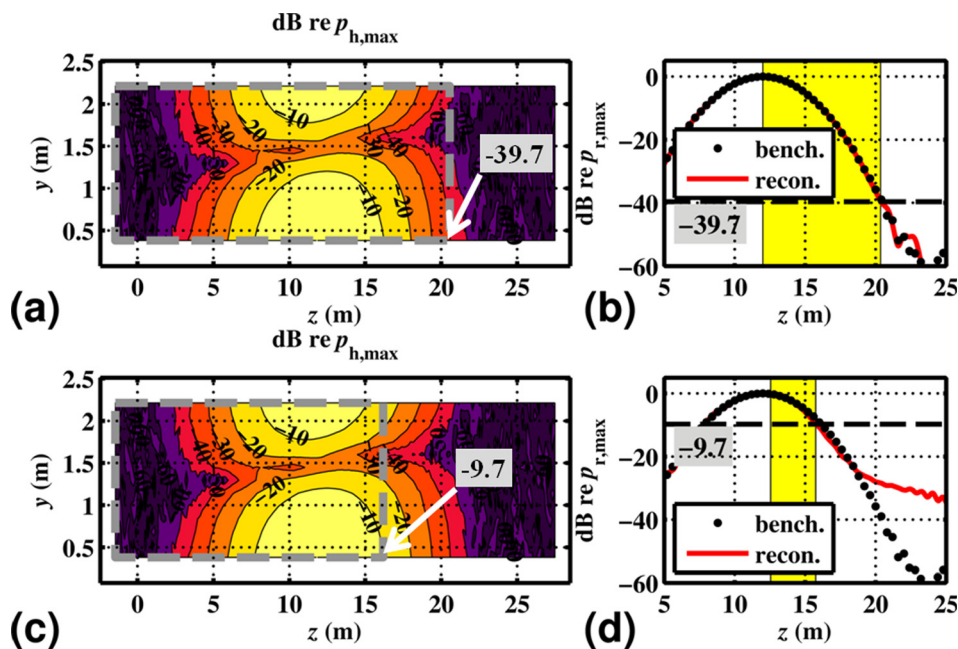


FIG. 13. (Color online) Numerical example to illustrate array aperture effects. A direct and image source consisting of lines of monopoles are used to simulate the sound field along the hologram plane at 250 Hz in (a) and (c) and near the source location, shown as dots in (b) and (d). Hologram levels are shown relative to the hologram maximum level, and contour lines are separated by 10 dB. Dashed rectangles indicate truncation boundaries. Parts (b) and (d) show the two respective source reconstructions (solid lines) compared with the benchmark (dots). Benchmark and reconstruction levels are shown relative to the reconstruction maximum. Truncation levels are indicated with a dashed line and a number. Highlighted areas indicate the data used in the error calculations.

Education through an interagency agreement between the U.S. Department of Energy and USAFRL.

## APPENDIX

A numerical study is shown here that helps to quantify the reconstruction errors of acoustic sources when benchmark data are not available. This simulation mimicked the coordinate system and relative source/measurement geometry of the full-scale jet measurement. A simulated sound field was generated using an array of 200 coherent monopoles 1.9 m above a reflecting surface. The spacing between monopoles was 1/10 of the acoustic wavelengths, and the line of monopoles was centered at  $z = 12$  m. A Gaussian weighting was applied to the monopole amplitudes with a function width of two acoustic wavelengths. The ground reflection was simulated by a second, or image source array at  $-1.9$  m (below the ground). Field pressures at the hologram locations were simulated using the Green's function for monopoles. Random noise was added to the data such that the signal-to-noise ratio, defined as the difference between the maximum hologram level and the level of the root-mean-squared value of the noise, was 60 dB.

The results are first demonstrated for a single frequency. The simulated field across the hologram surface for the 250-Hz case is shown in Fig. 13(a), and the benchmark, consisting of simulated field levels along the line  $x = 0.3$  m,  $y = 1.9$  m (close to the source) is shown by the dots in Fig. 13(b). The amplitudes in the simulated hologram and “source” fields are each in units of decibel with reference to their respective maximum root-mean-square pressures,  $p_{h,max}$  and  $p_{r,max}$ . Prior to M-SONAH processing, a selection of downstream columns of the hologram were removed. For example, the dashed rectangle in Fig. 13(a) shows that the hologram was effectively truncated at  $z = 20.6$  m. Holographic projection (using only the data within the rectangle) was identical to that of the jet data as

explained in Sec. III A—linear prediction was used to extend the aperture upstream and downstream, grid resolution was reduced, and the data were projected to the benchmarked source location using M-SONAH and the same EWM representation as previously. The source reconstruction is shown by the solid line in Fig. 13(b).

The maximum level (relative to the hologram maximum) along the right edge of the truncated hologram in Fig. 13(a) is  $-39.7$  dB and is referred to as the “truncation level.” In the reconstruction, the same truncation level (now relative to the reconstruction maximum) is shown by the dotted line in Fig. 13(b). The highlighted region in Fig. 13(b) shows the range in  $z$  between the reconstruction maximum and the point at which the reconstruction level drops to the truncation level. The maximum error between the benchmark numerical levels and the reconstructions above the truncated level (in the highlighted region) is 1.0 dB. To explore the effect of the truncation level on the reconstruction, a different portion of the hologram is used with a truncation level of  $-9.7$  dB, which is shown in Figs. 13(c) and 13(d). In this instance, the maximum error in the region greater than the truncation level is 0.4 dB but grows dramatically outside the highlighted region in Fig. 13(d). For both of the cases shown here, reconstructions from the source maximum down to the truncation level are highly accurate but may deviate outside this region.

To validate this criterion further, the preceding simulation was repeated for octave-band center frequencies from 63 to 1000 Hz and for several truncation levels from  $-50$  to 0 dB. In all cases, maximum reconstruction errors (above the truncation level) were less than 2 dB. Thus the range of SPL captured by the hologram indicates the range of levels that are well approximated by the reconstruction. That is, if the top 10 dB of energy is captured in the hologram, then errors in the top 10 dB of the source reconstruction are likely less than 2 dB. Based on this result, the jet source reconstructions to be shown in Sec. IV are probably accurate to within 2 dB.

- <sup>1</sup>A. Towne, T. Colonius, P. Jordan, A. Cavalieri, and G. A. Brès, "Stochastic and nonlinear forcing of wavepackets in a Mach 0.9 jet," *AIAA Paper 2015-2217* (2015).
- <sup>2</sup>M. Itasse, J. P. Brazier, O. Léon, and G. Casalis, "Nonlinear interaction analysis of subsonic jet instabilities with forced eigenmodes using PSE," *AIAA Paper 2015-3124* (2015).
- <sup>3</sup>J. D. Maynard, E. G. Williams, and Y. Lee, "Nearfield acoustic holography: 1. Theory of generalized holography and the development of NAH," *J. Acoust. Soc. Am.* **78**, 1395–1413 (1985).
- <sup>4</sup>E. Mollo-Christensen, "Jet noise and shear flow instability seen from an experimenter's viewpoint," *J. Applied Mech.* **34**, 1–7 (1967).
- <sup>5</sup>C. K. W. Tam, "Directional acoustic radiation from a supersonic jet generated by shear layer instability," *J. Fluid Mech.* **46**, 757–768 (1971).
- <sup>6</sup>C. K. W. Tam, "Mach wave radiation from high-speed jets," *AIAA J.* **47**, 2440–2448 (2009).
- <sup>7</sup>R. H. Schlinker, S. A. Liljenberg, D. R. Polak, K. A. Post, C. T. Chipman, and A. M. Stern, "Supersonic jet noise source characteristics and propagation: Engine and model scale," *AIAA Paper 2007-3623* (2007).
- <sup>8</sup>D. F. Long, "Jet noise source location via acoustic holography and shadowgraph imagery," *AIAA Paper 2008-2888* (2008).
- <sup>9</sup>D. F. Long, "Evaluation of jet and shock cell noise via acoustic holography," *AIAA Paper 2008-5* (2008).
- <sup>10</sup>S. S. Lee and J. Bridges, "Phased-array study of dual-flow jet noise: Effect of nozzles and mixers," *AIAA Paper 2006-2647* (2006).
- <sup>11</sup>A. T. Wall, K. L. Gee, M. M. James, K. A. Bradley, S. A. McNerny, and T. B. Neilsen, "Near-field noise measurements of a high-performance military jet aircraft," *Noise Control Eng. J.* **60**, 421–434 (2012).
- <sup>12</sup>B. M. Harker, K. L. Gee, T. B. Neilsen, A. T. Wall, and M. M. James, "Phased-array measurements of full-scale military jet noise," *AIAA Paper 2014-3069* (2014).
- <sup>13</sup>B. M. Harker, T. B. Neilsen, K. L. Gee, A. T. Wall, and M. M. James, "Spatiotemporal correlation analysis of jet noise from a high-performance military aircraft," *AIAA Paper 2015-2376* (2015).
- <sup>14</sup>D. M. Hart, T. B. Neilsen, K. L. Gee, and M. M. James, "A Bayesian based equivalent sound source model for a military jet aircraft," *Proc. Mtg. Acoust.* **19**, 055094 (2013).
- <sup>15</sup>T. A. Stout, K. L. Gee, T. B. Neilsen, A. T. Wall, and M. M. James, "Intensity analysis of the dominant frequencies of military jet aircraft noise," *Proc. Mtg. Acoust.* **20**, 040010 (2015).
- <sup>16</sup>T. B. Neilsen, K. L. Gee, A. T. Wall, and M. M. James, "Similarity spectra analysis of high-performance jet aircraft noise," *J. Acoust. Soc. Am.* **133**, 2116–2125 (2013).
- <sup>17</sup>D. F. Long, J. Peters, and M. Anderson, "Evaluating turbofan exhaust noise and source characteristics from near field measurements," *AIAA Paper 2009-3214* (2009).
- <sup>18</sup>P. N. Shah, H. Vold, and M. Yang, "Reconstruction of far-field noise using multireference acoustical holography measurements of high-speed jets," *AIAA Paper 2011-2772* (2011).
- <sup>19</sup>M. Lee and J. S. Bolton, "Source characterization of a subsonic jet by using near-field acoustical holography," *J. Acoust. Soc. Am.* **121**, 967–977 (2007).
- <sup>20</sup>H. Vold, P. N. Shah, J. Davis, P. G. Bremner, D. McLaughlin, P. Morris, J. Veltin, and R. McKinley, "High-resolution continuous scan acoustical holography applied to high-speed jet noise," *AIAA Paper 2010-3754* (2010).
- <sup>21</sup>A. T. Wall, K. L. Gee, T. B. Neilsen, D. W. Krueger, and M. M. James, "Cylindrical acoustical holography applied to full-scale jet noise," *J. Acoust. Soc. Am.* **136**, 1120–1128 (2014).
- <sup>22</sup>P. Jordan and T. Colonius, "Wave packets and turbulent jet noise," *Annu. Rev. Fluid Mech.* **45**, 173–195 (2013).
- <sup>23</sup>J. Hald, "STSF—a unique technique for scan-based near-field acoustic holography without restrictions on coherence," *Brüel and Kjer Technical Review No. 1-1989* (1989).
- <sup>24</sup>A. T. Wall, K. L. Gee, and T. B. Neilsen, "Multisource statistically optimized near-field acoustical holography," *J. Acoust. Soc. Am.* **137**, 963–975 (2015).
- <sup>25</sup>M. Lee and J. S. Bolton, "Scan-based near-field acoustical holography and partial field decomposition in the presence of noise and source level variation," *J. Acoust. Soc. Am.* **119**, 382–393 (2006).
- <sup>26</sup>S. M. Price and R. J. Bernhard, "Virtual coherence: A digital signal processing technique for incoherent source identification," in *Proceedings of Fourth International Modal Analysis Conference* (1980), pp. 1256–1262.
- <sup>27</sup>A. T. Wall, M. D. Gardner, K. L. Gee, and T. B. Neilsen, "Coherence length as a figure of merit in multireference near-field acoustical holography," *J. Acoust. Soc. Am.* **132**, EL215–EL221 (2012).
- <sup>28</sup>R. Steiner and J. Hald, "Near-field acoustical holography without the errors and limitations caused by the use of spatial DFT," *Int. J. Acoust. Vib.* **6**(2), 83–89 (2001).
- <sup>29</sup>A. T. Wall, K. L. Gee, D. W. Krueger, T. B. Neilsen, S. D. Sommerfeldt, and M. M. James, "Aperture extension for near-field acoustical holography of jet noise," *Proc. Mtg. Acoust.* **14**, 065001 (2012).
- <sup>30</sup>E. G. Williams, "Continuation of acoustic near-fields," *J. Acoust. Soc. Am.* **113**(3), 1273–1281 (2003).
- <sup>31</sup>L. B. Jackson, *Digital Filters and Signal Processing*, 2nd ed. (Kluwer Academic Publishers, Boston, 1989), pp. 255–257.
- <sup>32</sup>H. Vold, P. Shah, P. Morris, Y. Du, and D. Papamoschou, "Axisymmetry and azimuthal modes in jet noise," *AIAA Paper 2012-2214* (2012).
- <sup>33</sup>A. T. Wall, K. L. Gee, and T. B. Neilsen, "Modified statistically optimized near-field acoustical holography for jet noise characterization," *Proc. Mtg. Acoust.* **19**, 055013 (2013).
- <sup>34</sup>A. T. Wall, K. L. Gee, T. B. Neilsen, and M. M. James, "Acoustical holography imaging of full-scale jet noise fields," *Proc. Noise-Con 2013*.
- <sup>35</sup>D. K. McLaughlin, C.-W. Kuo, and D. Papamoschou, "Experiments on the effect of ground reflections on supersonic jet noise," *AIAA Paper 2008-22* (2008).
- <sup>36</sup>Y. T. Cho, J. S. Bolton, and J. Hald, "Source visualization by using statistically optimized near-field acoustical holography in cylindrical coordinates," *J. Acoust. Soc. Am.* **118**(4), 2355–2364 (2005).
- <sup>37</sup>J. Hald, "Basic theory and properties of statistically optimized near-field acoustical holography," *J. Acoust. Soc. Am.* **125**, 2105–2120 (2009).
- <sup>38</sup>J. Morgan, T. B. Neilsen, K. L. Gee, A. T. Wall, and M. M. James, "Simple-source model of military jet aircraft noise," *Noise Control Eng. J.* **60**(4), 435–449 (2012).
- <sup>39</sup>E. G. Williams, "Regularization methods for near-field acoustical holography," *J. Acoust. Soc. Am.* **110**, 1976–1988 (2001).
- <sup>40</sup>R. Reba, S. Narayanan, and T. Colonius, "Wave-packet models for large-scale mixing noise," *Int. J. Aeroacoust.* **9**, 533–558 (2010).
- <sup>41</sup>A. Sinha, D. Rodríguez, G. A. Brès, and T. Colonius, "Wavepacket model for supersonic jet noise," *J. Fluid Mech.* **742**, 71–95 (2014).
- <sup>42</sup>D. Papamoschou, "Wavepacket modeling of the jet noise source," *AIAA Paper 2011-2835* (2011).
- <sup>43</sup>T. B. Neilsen, K. L. Gee, B. M. Harker, and M. M. James, in "Level-educed wavepacket representation of noise radiation from a high-performance military aircraft," *AIAA Paper 2016-1880* (2016).
- <sup>44</sup>C. K. W. Tam and D. E. Burton, "Sound generated by instability waves of supersonic flows. Part 2. Axisymmetric jets," *J. Fluid Mech.* **138**, 273–295 (1984).
- <sup>45</sup>K. L. Gee, V. W. Sparrow, M. M. James, J. M. Downing, C. W. Hobbs, T. B. Gabrielson, and A. A. Atchley, "The role of nonlinear effects in the propagation of noise from high-power jet aircraft," *J. Acoust. Soc. Am.* **123**, 4082–4093 (2008).
- <sup>46</sup>C. E. Tinney, M. N. Glauser, and L. S. Ukeiley, "Low-dimensional characteristics of a transonic jet. Part 1. Proper orthogonal decomposition," *J. Fluid Mech.* **612**, 107–141 (2008).
- <sup>47</sup>B. Greska and A. Krothapalli, "On the far-field propagation of high-speed jet noise," in *Proceedings of NCAD/NoiseCon2008* (2008), No. NCAD2008-73071.
- <sup>48</sup>T. D. Norum, D. P. Garber, R. A. Golub, O. L. Santa Maria, and J. S. Orme, "Supersonic jet exhaust noise at high subsonic flight speed," *NASA/TP-2004-212686* (2004).
- <sup>49</sup>C. K. W. Tam and S. A. Parrish, "Noise of high-performance aircraft at afterburner," *J. Sound Vib.* **352**, 103–208 (2015).
- <sup>50</sup>J. Liu, A. Corrigan, K. Kailasanath, and E. Gutmark, "Impact of chevrons on noise source characteristics in imperfectly expanded jet flows," *AIAA Paper 2015-2835* (2015).
- <sup>51</sup>J. Liu, A. Corrigan, K. Kailasanath, and B. Taylor, "Impact of the specific heat ratio on noise generation in a high-temperature supersonic jet," *AIAA Paper 2016-2125* (2016).
- <sup>52</sup>A. T. Wall, K. L. Gee, T. B. Neilsen, B. M. Harker, S. A. McNerny, R. L. McKinley, and M. M. James, "Investigation of multi-lobed fighter jet noise sources using acoustical holography and partial field decomposition methods," *AIAA Paper 2015-2379* (2015).